Optical Filtering for Near Field Photometry with High Order Basis

Xavier Granier, Michael Goesele, Wolfgang Heidrich, Hans-Peter Seidel

INSTITUT NATIONAL DE RECHERCHE EN INFORMATIQUE ET EN AUTOMATIQUE

Optical Filtering for Near Field Photometry with High Order Basis

Xavier Granier — Michael Goesele — Wolfgang Heidrich — Hans-Peter Seidel

N° 6000

October 2006

Thème COG

ISSN 0249-6399 ISRN INRIA/RR--6000--FR+ENG

Optical Filtering for Near Field Photometry with High Order Basis

Xavier Granier* , Michael Goesele† , Wolfgang Heidrich‡ , Hans-Peter Seidel§

Thème COG — Systèmes cognitifs
Projet IPARLA

Rapport de recherche n° 6000 — October 2006 — 23 pages

Abstract: Accurately capturing the near field emission of complex luminaires is still very difficult. In this paper, we describe a new acquisition pipeline of such luminaires that performs an orthogonal projection on a given basis in a two-step procedure. First, we use an optical low-pass filter that corresponds to the reconstruction basis to guarantee high precision measurements. The second step is a numerical process on the acquired data that finalizes the projection. Based on this concept, we introduce new experimental setups for automatic acquisition and perform a detailed error analysis of the acquisition process.

Key-words: Light Sources Acquisition; Optical Filtering; Error Analysis

* IPARLA project (LaBRI - INRIA futurs)
† University of Washington
‡ The University of British Columbia
§ Max Plank Institüt für Informatik

Unité de recherche INRIA Futurs
Parc Club Orsay Université, ZAC des Vignes,
4, rue Jacques Monod, 91893 ORSAY Cedex (France)
Téléphone : +33 1 72 92 59 00 — Télécopie : +33 1 60 19 66 08

Filtrage Optique pour l'Acquisition Photométrique d'un Champ Proche dans des Bases d'Ordre Elevé

Résumé : La mesure précise du champ proche des luminaires est toujours très difficile. Dans ce rapport, nous présentons une nouvelle procédure d'acquisition de ces sources de lumières qui effectue une projection orthogonale dans une base prédéfinie, et ce par une procédure en deux étapes. Premièrement, nous utilisons un filtre optique passe-bas correspondant à la base de reconstruction. Ceci garantit une mesure de haute précision. La seconde étape est une processus numérique sur les données acquises qui finalise la projection orthogonale dans le base reconstruction. Basé sur ce concept, nous introduisons de nouveaux systèmes expérimentaux d'acquisition et nous présentons une étude détaillée des erreurs correspondantes.

Mots-clés : Acquisition de sources de lumières; Filtrage optique; Analyse d'Erreur

1 Introduction

1.1 Motivation

For lighting simulation and design, the light source model has a major influence on the accuracy of the simulation [CJM02]. Unfortunately, the direct simulation approach is often not feasible, since the required data is rarely available for real light sources, since accurate modeling of a real luminaire is difficult and inaccurate parameters such as the glass thickness of a halogen light bulbs can have a significant impact on the luminaire's emission pattern; and finally, a complete rendering of a scene including a full simulation of the light emission and transport inside the luminaire is generally complex and therefore very time and resource consuming.

Incorporating measured light emission data from complex luminaires into a rendering system provides a solution to this problem. The luminaire is generally approximated by a point light source [SB90] and therefore many companies provide goniometric diagrams [VG84], which describe their far field (i.e., light emission from a point light source parameterized by emission direction).

Unfortunately, the far field is only a faithful approximation of the emitted light when the light source is sufficiently far away from the object to be illuminated – as a rule of thumb at least five times the maximum luminaire dimension [Ash95]. All effects requiring knowledge of the spatial and directional light emission can only be modeled by a near field representation such as a light field [GGSC96, LH96]. It represents the luminaire's emission without knowledge of its geometry or internal structure.

1.2 Previous Work

Several approaches to measure the near field emission of a luminaire have been developed in recent years. Ashdown [Ash93, Ash95] pointed a number of cameras at a luminaire (or, more practically, a single camera is moved around on a robot arm) and recorded the irradiance incident on an imaging sensor. Both Rykowski and Wooley [RW97], and Jenkins and Mönch [JM00] employ a similar setup to acquire the light field of a luminaire, while Siegel and Stock [SS96] replaced the camera lens with a pinhole.

In all these approaches, the camera positions correspond to a sampling of some virtual surface $\mathcal{S}$. In practice, the luminaire may produce arbitrarily high spatial frequencies on $\mathcal{S}$. Even with a good sampling strategy [CCST00], aliasing is introduced unless a low-pass filter is applied before the sampling step. This issue has been raised by Halle [Hal94] and was noted by Levoy and Hanrahan [LH96]. They all propose to use the finite aperture of the camera lens as a low-pass filter by choosing the aperture size equal to the size of a sample on the camera plane. The properties of the low-pass filter are dependent on the lens system, and can not be user-defined. No further control on the process is possible. As an example, we can not guarantee the continuity of the final reconstruction when using these approaches.

To address this problem, Goesele et al. [GGHS03] introduced a new acquisition approach based on an optical low-pass filter. This filter performs a projection of the luminaire's near field on a predefined basis.

1.3 Overview and Contributions

This paper introduces two acquisition setups for a new acquisition pipeline and the new design of the corresponding optical filters. The acquisition pipeline is a two-step process: the light source is first optically filtered. Then the acquired images are numerically transformed, to finish the projection of the light source in the pre-defined basis. The design of the filter is based on a detailed error study, also presented in this paper. It shows the resulting errors for the different approximations that are needed to produce a feasible setup.

The remainder of this paper is organized as follows: first, we summarize the general approach for light source acquisition [GGHS03]. Then, we introduce our new filtering approach in Section 3 that simplifies the acquisition but requires a basis transformation of the measured data. In Section 4, we describe the setups of our experiments including a planer and a cylindrical configuration. Then we analyze the error introduced by the cylindrical configuration (Section 5). We finally show some acquisitions of real luminaires (Section 6) before we conclude.

2 Theory

2.1 Basic Approach

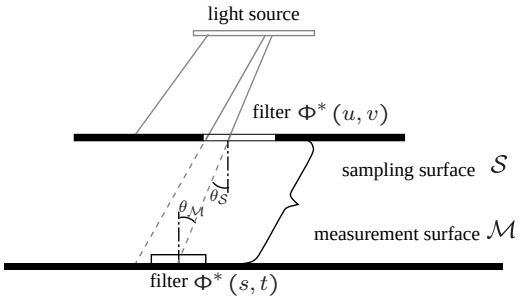

Figure 1: Cross section through the conceptual acquisition setup.

The conceptual setup for our approach to filtered light source measurement is depicted in Figure 1. Light rays are emitted from the light source and hit a filter in a surface $\mathcal{S}$. This surface is opaque except for the finite support area of the filter that can be moved to a number of discrete positions on a regular grid. The filter is a semi-transparent film, similar to a slide, containing the 2D image of a function $\Phi^*_{ij}(u,v)$. The finite support is required

Table 1: Notation (overview) – see also Figure 1.

Symbol	Meaning
$\Psi_{ijkl}\,(u,v,s,t)$	basis function for approximating the light field
Φ_i	1D basis used for reconstruction
$\Phi_{ijkl}\,(u,v,s,t)$	4D tensor product basis for reconstruction
Φ_i^*	biorthogonal 1D basis used for measurement
$\Phi_{ijkl}^*\,(u,v,s,t)$	4D tensor product basis for measurement
$\mathcal{M}$	surface on which the irradiance is measured ((s,t)-surface)
$\mathcal{S}$	surface on which the optical filters are placed ((u,v)-surface)
$L(u,v,s,t)$	radiance passing through (u,v) on $\mathcal{S}$ and (s,t) on $\mathcal{M}$
$\tilde{L}(u,v,s,t)$	projection of $L(u,v,s,t)$ into basis $\{\Psi_{ijkl}\,(u,v,s,t)\}$
$L_{mn}(u,v,s,t)$	radiance $L(u,v,s,t)\Phi_{mn}^*\,(u,v)$ filtered with $\Phi_{mn}^*\,(u,v)$
$E_{mn}(s,t)$	irradiance caused by $L_{mn}(u,v,s,t)$ on the surface $\mathcal{M}$

to allow a physical setup. The light falling through this filter is attenuated according to $\Phi_{ij}^*\,(uv)$ and hits a second surface $\mathcal{M}$, on which we are able to measure the irradiance with a high spatial resolution.

The fundamental difference to previous work [Ash93, SS96] is that we can select an arbitrary filter $\Phi_{ij}^*\,(u,v)$ depending on the arbitrarily chosen function space into which we want to project the light field emitted by the luminaire. This results in an optical low-pass filtering of the light field *before* sampling, and thus helps avoiding aliasing artifacts.

In principle, one also has to perform low-pass filtering on the measurement surface $\mathcal{M}$. This, however, is optically very difficult or even impossible to implement when the filter kernels overlap. Nevertheless, it is technically easy to achieve a very high measurement resolution on $\mathcal{M}$, so that we can consider the measured data as point samples, and implement an arbitrary filter kernel while downsampling to the final resolution. Note that the filter kernels for $\mathcal{S}$ and $\mathcal{M}$ can be chosen independently as required by the reconstruction process.

2.2 Light Source Representation

Before we discuss the theory behind the proposed method in detail, we first introduce the mathematical notation used throughout this document (summarized in Figure 1 and Table 1).

For the measurement, we assume that the light field emitted by the light source is well represented by a projection into a basis $\{\Psi_{ijkl}\,(u,v,s,t)\}_{ijkl\in\mathbb{Z}}$ (similar to the lumigraph [GGSC96]):

$$L(u,v,s,t) \approx \tilde{L}(u,v,s,t) := \sum_{i,j,k,l} L_{ijkl}\Psi_{ijkl}\,(u,v,s,t)\,. \tag{1}$$

We assume that Ψ_{ijkl} has local support, and i, j, k, and l roughly correspond to translations in u, v, s, and t, respectively. We also define two additional sets of basis functions, one

for *measuring* and one for *reconstruction*. For reconstruction, we use a 1D basis $\{\Phi_i\}_{i\in\mathbb{Z}}$ with the property $\Phi_i(x) = \Phi(x+i)$. The 4D reconstruction basis is then given as the tensor product basis

$$\Phi_{ijkl}(u,v,s,t) := \Phi_i(u)\,\Phi_j(v)\,\Phi_k(s)\,\Phi_l(t).$$

For measurement, we use the *biorthogonal* (or *dual*) $\{\Phi_i^*(x)\}_{i\in\mathbb{Z}}$ of the reconstruction basis defined by

$$\langle \Phi_i^* \cdot \Phi_{i'} \rangle = \int_{-\infty}^{\infty} \Phi_i^*(x)\,\Phi_{i'}(x)\; dx = \delta_{i,i'} \tag{2}$$

- where the Kronecker's symbol $\delta_{i,i'} = 1$ if $i = i'$, and $\delta_{i,i'} = 0$ otherwise - and again we perform tensor-product construction for the 4D measurement basis.

2.3 Measured Irradiance

Our approach is based on measuring the irradiance $E_{mn}(s,t)$ on the measurement surface $\mathcal{M}$ (parameterized by (s,t)) that is caused by the incident radiance $L(u,v,s,t)\Phi_{mn}^*(u,v)$:

$$E_{mn}(s,t) = \int_{-\infty}^{\infty}\int_{-\infty}^{\infty} g(u,v,s,t)\,L(u,v,s,t)\Phi_{mn}^*(u,v)\; du\,dv \tag{3}$$

$$\approx \sum_{i,j,k,l} L_{ijkl} \int_{-\infty}^{\infty}\int_{-\infty}^{\infty} g(u,v,s,t)\,\Psi_{ijkl}(u,v,s,t)\,\Phi_{mn}^*(u,v)\; du\,dv. \tag{4}$$

The geometric term $g(u,v,s,t)$ is defined as

$$g(u,v,s,t) = \frac{\cos\theta_{\mathcal{S}}\cos\theta_{\mathcal{M}}}{d^2}. \tag{5}$$

where d is the distance between the point (u,v) on the sampling surface $\mathcal{S}$ and the point (s,t) on the sampling surface $\mathcal{M}$. $\theta_{\mathcal{S}}$ and $\theta_{\mathcal{M}}$ are the angles between the normals of $\mathcal{S}$ and $\mathcal{M}$ and the vector connecting (u,v) and (s,t), respectively. Note that g also accounts for any differences in the parameterization on the two surfaces (i.e., different grid spacing). When $\mathcal{S}$ and $\mathcal{M}$ are parallel, $g = \cos^2\theta/d^2$, since $\theta_{\mathcal{S}} = \theta_{\mathcal{M}} = \theta$.

2.4 Reconstruction

We now describe an exact reconstruction algorithm from the measurements E_{mn}. To this end, we first define what the relationship between the basis functions Ψ_{ijkl} and the reconstruction and measurement bases should be. We define

$$\Psi_{ijkl}(u,v,s,t) := \frac{1}{g(u,v,s,t)}\Phi_{ij}(u,v)\,\Phi_{kl}(s,t). \tag{6}$$

From Equation 4 and the biorthogonality relationship (Equation 2) follows

$$E_{mn}(s,t) = \sum_k \sum_l L_{mnkl}\Phi_{kl}(s,t). \tag{7}$$

In order to determine which reconstruction filter to use, we rewrite Equation 1 using Equations 6 and 7:

$$\tilde{L}(u,v,s,t) = \sum_{m,n,k,l} L_{mnkl}\Psi_{mnkl}(u,v,s,t) = \sum_{m,n} \frac{1}{g(u,v,s,t)}\Phi_{mn}(u,v)\,E_{mn}(s,t). \quad (8)$$

This indicates that we can *exactly* reconstruct $\tilde{L}$, the projection of L into the basis $\{\Psi_{ijkl}\}$, by using the reconstruction filter $\Phi_{mn}(u,v)/g(u,v,s,t)$.

Based on Equations 8 and 3, as well as the biorthogonality relationship (Equation 2), the coefficients L_{mnkl} are defined as

$$\begin{aligned} L_{mnkl} &= \int_{-\infty}^{\infty}\int_{-\infty}^{\infty} E_{mn}(s,t)\,\Phi^*_{kl}(s,t)\,ds\,dt \\ &= \int_{-\infty}^{\infty}\int_{-\infty}^{\infty}\int_{-\infty}^{\infty}\int_{-\infty}^{\infty} g(u,v,s,t)\,L(u,v,s,t)\Phi^*_{mn}(u,v)\,\Phi^*_{kl}(s,t)\,du\,dv\,ds\,dt \end{aligned} \quad (9)$$

corresponding to the energy measured at a position on the measurement surface.

3 Filter design

3.1 Criteria for Selecting Bases and Filters

We propose two main criteria for the filter design. First, for practical reasons, it is preferable to use a single filter for all positions on $\mathcal{S}$ (i.e., $\Phi^*_i = \Phi^*_{i'}$).

Furthermore, the choice of a basis (and then of a filter) should depend on the intended application. For example, using the acquired light sources for image synthesis, the basis should be at least $\mathcal{C}^1$ continuous, since the human's visual system is sensible to both $\mathcal{C}^0$- and $\mathcal{C}^1$-discontinuities [LaDP99]. This is our second criteria.

The posssibility of selecting context-based proterty for both our filter (and thus our reconstruction basis) is the main difference with the previous work.

3.2 Dual Basis for an Orthogonal Projection

The theoretical setup as presented in Section 2.2 uses a dual basis as filter. A dual basis $\{\Phi^*_i\}$ – as described in Equation 2 – defines a projection into the basis $\{\Phi_i\}$. Thus, the projection $\tilde{f}$ of f is: $\tilde{f} = \sum_i \langle \Phi^*_i \cdot f \rangle \Phi_i$ Since a basis and its dual span the same function space, the individual basis functions Φ^*_i of the dual can be expressed as linear combinations of the primary basis: $\Phi^*_i = \sum_j a_{ij}\Phi_j$ Using Equation 2, we obtain the following conditions: $\langle \Phi^*_i \cdot \Phi_i \rangle = \sum_j a_{ij} \langle \Phi_j \cdot \Phi_k \rangle = \delta_{ik}$ Thus, the (a_{ij}) coefficients can be computed by inverting the symmetric matrix $(\langle \Phi_i \cdot \Phi_j \rangle)_{ij}$.

Unfortunately, using directly the dual function as a filter has several downsides for the realization of a working setup. First, for a positive primary basis, the dual function usually has both positive and negative function values (see Figure 2). One solution would be to create

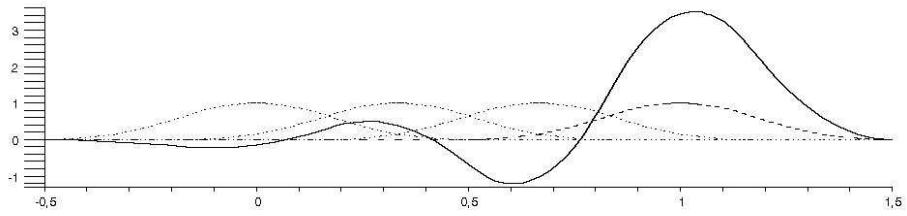

Figure 2: Four quadratic B-splines (dotted line) and one dual function (plain line). The dual corresponds to the rightmost B-spline function (both in bold).

two filters, one representing the positive part of the dual only, and the other representing the negative part[GGHS03]. A measurement session will then need two passes, with some possible alignment problems between the two acquisitions.

A second problem is that the duals usually have a large support (corresponding to a large number of non-zero coefficients (a_{ij})). In practice, this can be addressed by restricting the support of the dual basis functions, effectively setting most of the (a_{ij}) to zero. Obviously this introduces an approximation error.

The final problem is that, for a finite basis, the duals are in general not exact and shifted copies of each other, even if the primary basis functions are. This would require the creation of different optical filters for different positions, which is not feasible in practice.

3.3 Using the Primary Basis as a Filter

To overcome all these issues, we directly use the primary basis as a filter for the measurement process. The dual representation is then computed software as

$$\langle \Phi_i^* \cdot f \rangle = \sum_j a_{i,j} \langle \Phi_j \cdot f \rangle .$$

This approach has several advantages. First, we have complete control over the filter support. Second, for any primary basis defined by a positive function, only one filter is required. Then, all filters are now exact copies of each other and thus fit our first criterion (see Section 3.1). In particular, they are also independent of the measurement domain, which means that we can now extend the domain without having to repeat previous measurements with new filters. Finally, this approach reduces the filter support for a given reconstruction resolution.

With this new experimental setup, we are now free to use a wide variety of different filters. In our experiments we use quadratic B-Splines, since there are simple filters that fulfill the continuity criterion outlined in Section 3.1.

Unfortunately, the linear combination introduced with this new filter design can be time consuming. When the size of the reconstruction basis on the filter planes is N, a maximum of $\mathcal{O}(N)$ linear combinations is required to compute the measure corresponding to each

basis function. Hence, the complexity of this step is then $\mathcal{O}\left((N \times M)^2\right)$ where $N \times M$ is the number of acquired images.

Fortunately, the absolute values of the dual basis coefficients (i.e., the $|a_{ij}|$ described in Section 3.2) decrease quickly. With only 14 coefficients the resulting error on the acquired data is below 0.5% for the 1D dual of a quadratic B-Spline (the equivalent of a 1% error for the 2D case). By keeping the number of coefficients under 14, the complexity of this step is linear.

Note that this error corresponds to a measure of a constant light source through the equivalent dual filter (after the linear combination). This is a very conservative upper bound. It is lower for the dual basis at the border of the domain.

Hence, the linear combination introduces also some flexibility in the final quality of the acquisition: a first approximation can be done quickly with a low number of coefficients and the high quality solution can be computed later.

4 Automatic Acquisition Setup

4.1 Generic Planar Configuration

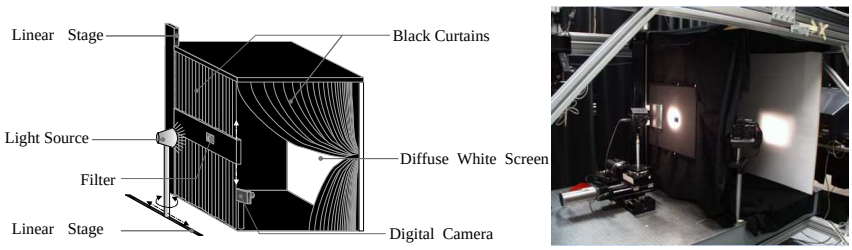

Figure 3: Physical setup

As a manual acquisition of a large number of measures can be very time consuming and prone to errors, we designed a setup based on the ACME [PLL+99] facility for an automatic acquisition (see Figure 3). We have developed two different configurations, the first one with two parallel planes as measurement and filter planes, and the second one with two coaxial cylindrical planes.

Due to the design, the fixed component of the setup is the measurement plane (a white screen, mate painted in order to create a diffuse screen). A camera facing this screen is our measurement device. Due to the build-in limitation in intensity range of a digital camera, we have to take several pictures with different exposure time for one position of the filter and of the light source, in order to reconstruct "High Dynamic Range" (HDR) images [DM97, RBS99]. With this approach, we can recover the real intensity of the light falling on the measurement plane.

For each new measure, the filter has to be shifted horizontally and vertically. The vertical translation is achieved by a vertical linear stage, on which the support of the filter is fixed. The movement of the measured light source, mounted on a horizontally linear stage, simulates the horizontal translation.

The acquisition setup is also isolated from any other incoming light. Some dark curtains are placed to create a black box around the white screen. In this black box, a camera is facing the screen. This guarantees that the measure data is perturbed by some inter-reflections. Also, in order to remove all lights other than the measured light source, the measurements take place in a dark room.

After the physical acquisition, a linear combination of the images is performed (see Section 3.3) in order to finalize the projection on the selected basis.

4.2 Cylindrical Configuration

Still, a planar configuration has a built-in limitation: when the filter is moving away from the optical axis, the measured solid angle is decreasing. A light source with an angular range larger than 180^o cannot be captured completely.

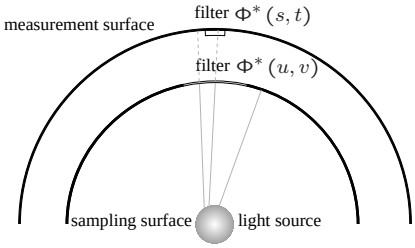

Figure 4: The theoretical cylindrical setup

The natural configuration to overcome this problem (a spherical setup around the light source) is very difficult to design: the filter has to be curved and cannot be easily designed to be unique and to be shifted over the sphere with a guarantee of $\mathcal{C}^1$ continuity. Instead, we introduce a cylindrical setup (see Figure 4). Thanks to the distortion-free mapping from a plane to a cylinder, the filter design is similar to the planar case. With this approach, we can capture all the emitting directions of a light source around the cylinder axis.

Unfortunately, a cylindrical measurement screen is also more complex to create than the corresponding planar ones. For our experiments, we approximate the cylinders by a set of tangent planes (see Figure 5). To achieve this configuration, the light source is mounted on a rotation stage, instead of the horizontal linear stage in the planar case (see Figure 3).

Similarly, we have to approximate the cylindrical filter with a planar one. The design of this new filter and the resulting errors are detailed in the following section.

After the physical acquisition, we reproject the HDR images on the cylinder in order to correct the planar approximation of the measurement screen. The resulting error are

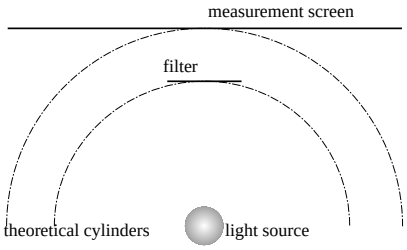

Figure 5: The practical cylindrical setup

detailed in Section 5.2. Then, like for the planar configuration, a linear combination of the images is performed.

5 Error Study for the Cylindrical Configuration

5.1 Filter Approximation

There are two main aspects in the design of this new filter: the projection from the cylinder to the approximating plane, and the position of this plane relative to the cylinder. We present now these different aspects.

5.1.1 Expression of the Parallax Error

The error resulting from the planar approximation $\psi(u,v)$ of the filter is due to the parallax. For a given ray, emitted from the light source and traversing the filter, the error is $\delta_P(u,v,s,t) = \psi(P(u,v,s,t)) - \psi(u,v)$, where P is the parallax due to the projection scheme. Hence, the error on the measured irradiance (see the Equation 3) is

$$E'(s,t) - E(s,t) = \int_{-\infty}^{\infty}\int_{-\infty}^{\infty} \frac{\cos^2\theta(u,v,s,t)}{R(u,v,s,t)^2}\delta_P(u,v,s,t)\, L(u,v,s,t)\ D\ dv,$$

This error can be bounded by $|E'(s,t) - E(s,t)| \leq \delta_P^{max}(s,t)\,\bar{E}(s,t)$ where $\delta_P^{max}(s,t) = max_{L(u,v,s,t)>0}\{|\delta_P(u,v,s,t)|\}$ represent the maximum parallax deviation from all incoming direction from the light source and $\bar{E}(s,t)$ is the measured irradiance with a constant filter. Note that δ_P^{max} depends on the relative size of the light source compared to the measurement setup. Intuitively, for a point light source, the parallax error has less influence than for an extended one.

Then, the resulting error on the measured coefficients of the light source is

$$\begin{aligned} |L - L'| &= \left| \int_{-\infty}^{\infty}\int_{-\infty}^{\infty} \Phi^*(s,t)\,(E(s,t) - E'(s,t))\ ds\ dt \right| \\ &\leq \|\delta\|\, max_{\Phi^*(s,t)>0}\left(\bar{E}\{s,t\}\right). \end{aligned}$$

In this Equation, $\|\delta\| = max_{\Phi^*(s,t)>0} \{\delta_P^{max}(s,t)\}$.

Hence, studying the error due to the approximate planar filter leads to study the maximum parallax error. This is the main focus of the following sections.

Note that, for a given reconstruction basis Φ, using the basis as a filter will greatly reduce the parallax error, since the support size will be smaller (about 14 times smaller for a good approximation of the dual - see Section 3.3).

5.1.2 Different projection schemes

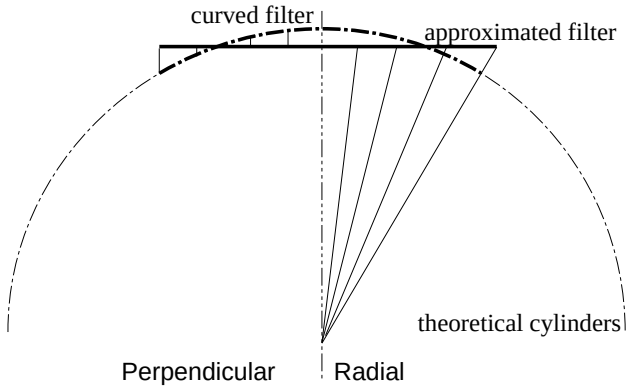

Figure 6: Perpendicular and radial projections

Since we are using a planar approximation of the filter, we have to project the curved filter on the planar one. We study two projections: a perpendicular projection and a radial projection (see Figure 6). As a reference, we also add the filter for the planar setup used here in a cylindrical context.

The projected filters and the non-projected one (see Table 2) filters converge to a similar behavior when the filter size is decreasing: the choice of the projection does not change significantly the error for small filters. The radial projection is the most accurate for all the configurations. It is our generic choice for the filter design.

5.1.3 Different filter positions

We study here two extreme positions for the approximate planar filter, as described in Figure 7. The first position is tangent to the theoretical cylinder; the second - the inner position - correspond to the case where the extremities of the approximate planar filter are on the cylinder.

The inner position requires a smaller filter (for a radial projection) so it seems to be interesting. However, the distance between the curved filter and the approximate planar filter is maximal in the center, where the values of the filter are the most important. Thus,

Table 2: Comparison of the maximum parallax error

filter aperture	$3\pi/5$	$3\pi/10$	$3\pi/20$	$3\pi/40$	$3\pi/80$
	tangent position				
radial proj.	21%	5%	3.8%	2.3%	1.22%
un-projected filter	17.6%	7%	4.2%	2.4%	1.23%
perpendicular proj.		8%	4.3%	2.5%	1.24%
	inner position				
radial proj.	84%	28%	16.8%	9.4%	5%
perpendicular proj.	56%	32%	17.8%	9.7%	5.1%

The comparison is done for perpendicular and radial projection, and for non-projected filter. The inner cylinder has a radius of 70cm and the distance between the two cylindrical surfaces is 30cm. Only the aperture of the theoretical filter is varying. We suppose that inner radius bounds the size of the light source.

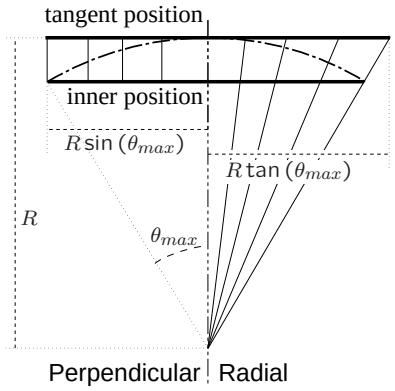

Figure 7: Filter position

the resulting parallax error is then larger (see Table 2). On the other hand, with the tangent position, the distance between the two filters is small in the center and higher toward the ends where the values of the filter are almost zero.

Consequently the tangent position should be chosen compared ti the other one, and this fact is confirmed by the numerical results (see Table 2).

5.2 Reprojection on the Measurement Surface

The cylindrical measurement surface is also approximated by a planar screen. The acquired measures need then to be reprojected in order create a real cylindrical configuration, while

introducing another error that is detailed in this section. We first present how the reprojection is performed.

5.2.1 Corrective Factor and Error Expression

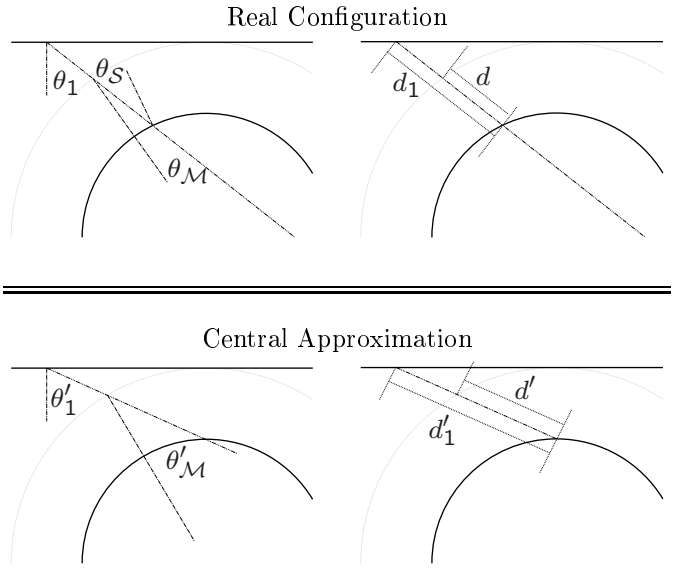

Figure 8: Reprojection configuration on the measurement screen

Instead of the theoretical measured coefficients (see Equation 9), the planar approximation of the measurement screen provides (using the notions of Figure 8, and assuming that the basis functions on the measurement surface are the same in both cases):

$$L'_{mnpq} = \int_{-\infty}^{\infty}\int_{-\infty}^{\infty}\int_{-\infty}^{\infty}\int_{-\infty}^{\infty} \frac{\cos\theta_1 \cos\theta_S}{{d_1}^2} L(u,v,s,t)\Phi^*_{mn}(u,v)\,\Phi^*_{pq}(s,t)\,du\;dv\;ds\;dt.$$

For the reprojection step, each acquired coefficient is scaled by a geometrical correction term λ_{mnpq}. the resulting error between the corrected coefficient and the theoretical one is:

$$\left|L_{mnpq} - \lambda L'_{mnpq}\right| \leq max_{uv\in filter, st\in pixel}\left|1 - \lambda_{mnpq}\frac{{d_1}^2\cos\theta_{\mathcal{M}}}{d^2\cos\theta_1}\right| |L_{mnpq}| = \epsilon\,|L_{mnpq}|$$

When the filter size and the pixel size of a measure are relatively small compared to the distance between the sampling plane and the measurement plane, the value of d_1 (resp. d, θ_1, θ_S, θ_M) is not varying a lot compared to the central value d'_1 (reps. d', θ'_1, θ'_1, θ'_M). λ

Table 3: Influence of different factors for the error on the reprojection.

Original	Light= $\frac{R}{2}$	Light= 0	$D = R$	$D = 4R$	aperture= $\frac{3\pi}{20}$	aperture= $\frac{3\pi}{80}$
5%	6.2%	3.8%	10.4%	2.4%	20%	3.2%

The original configuration is the following: the radius of the light source is $R/8$ (where R is the radius of the filtering cylinder), the filter aperture is $\frac{\Pi}{20}$, the distance D between the filter and the measurement screen is $2R$. The other column represent the change compared to the original setup.

is selected that there is no error on the ray defined by the center of the filter and the center of the pixel:

$$\lambda_{mnpq} = \frac{{d'}^2 \cos\theta'_1}{{d'_1}^2 \cos\theta'_{\mathcal{M}}}. \tag{10}$$

We design the reprojection step as follows. Each pixel of the acquired image is corrected by the scaling factor defined in Equation 10. The resulting image corresponds to an acquisition on a cylinder surface, but with non-regular pixels (each one corresponding to the projection of the original planar pixel on the cylinder). Thus, the image is finally resampled on a regular grid on the cylindrical surface.

5.2.2 Some Numerical Results

The results shown in Table 3 confirm some of our intuitions. First, the error increases significantly with the width of the filter (see the two last columns). Once again using the dual filter we dramatically increases the final error, as shown in Section 3.3, the dual is at least 14 times larger than the reconstruction basis. The solution is to reduce the size of the dual filter, leading to smaller basis function and to an increase of the measurement number to cover the same light source. Using the basis is still the best choice for the cylindrical acquisition.

Second, increasing the distance between the filter and the screen can help also in reducing the error, as it relatively reduces the size of the pixel and of the filter. But for the same directional coverage, the size of the screen has to increase also, leading to non-practicable setups.

Then, by adjusting these two factors, we can reach an error ϵ around 6% with a reasonable setup: the filter aperture is $\frac{\pi}{10}$, the distance between the filter and the screen is around twice the distance between the light and the filter, and the radius of the light source is below half of the radius of the filter.

5.3 Conclusion

In the cylindrical case, the planar approximation can create large errors, but they can be reduced by a careful design. There are principally three controls: (i) the filter size/aperture

Table 4: Common configuration for our experiments

distance light source — filter:	30cm
distance filter — screen:	75cm
screen size (width×height):	120cm×100cm
resolution of acquired images (width×height):	960×840

can be reduced - this reduces both the parallax and the reprojection error, (ii) the relative size of the light source can be reduced by scaling up the complete setup - that would reduce the error on the filter but not significantly the error on the screen -, (iii) the distance between the filter and the screen can be increased - this reduces mostly the reprojection error -.

When the positions of the light source, the position of the screen and the size of the filter are given, the only parameter is the filter position. On one hand, moving the filter closer to the screen has the three following effects. (i) Since this reduces the aperture, and this increases the required number of measures. Both errors on the screen and on the filter are reduced. (ii) This also reduces the size of the light compared to the size of the theoretical cylinder of the filter, while reducing both errors as well. (iii) But, this reduces the distance between the filter and the screen, and that increases the reprojection error (which is the larger of the two errors).

On the other hand, when the filter is closer to the light source, the parallax error is increased and reaches its maximum value. But this error is the smaller of the two. Consequently, the best solution is to put the filter closer to the light source than to the screen. This has been taken into account for designing the experimental setup described in the next Section.

Hence, the basis filter seems even more to be the best choice in the cylindrical setup, since it reduces the filter support for a given reconstruction resolution (see Section 3.3). With small filters, all the approximations are valid.

6 Acquired Data

In order to validate our results, we acquired a light source (a car headlight) with both geometric configurations (cylindrical and planar) and varying filter sizes. Table 4 shows the resolution of the acquired images and the geometric configuration of the setup. The setup was determined by the results of the error study presented in the previous section and constrained by the dimension of the ACME measurement facility. The filters were printed with 1016 dpi resolution on high-density film using a calibrated LightJet 2080 Digital Film Recorder. This produces slides with a dynamic range of more than $1:50{,}000$. The images were captured with a Jenoptik C14 digital camera. The filter (see Section 3) used for the experiments is based on a quadratic B-Spline function, with two different sizes: a large one (136.5mm) and a smaller one (49.14mm).

6.1 Cylindrical Acquisition

For the cylindrical acquisition, we first experiment the large filter (136.5mm). Based on the error study, we select a radial projection and a tangent position of the filter (see Section 5.1). With this large filter, only an array of 9×7 (angle×height) images was needed to cover the complete light source. This results in 194 MBytes of data.

Since the bounding sphere of the light source has a radius less than 20cm, the theoretical maximum parallax error is 3.7%. For the perpendicular projection, the theoretical error is 4.4% and 4.2% for a non-projected filter. Once again, the radial projection is better.

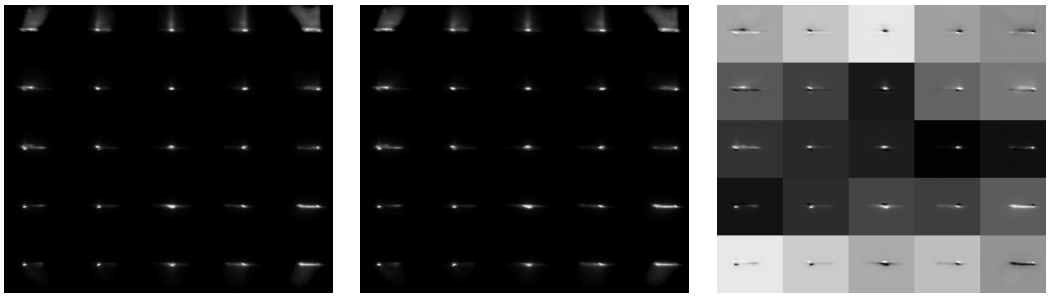

Figure 9: Some acquired data (left) and the corresponding images after the cylindrical projection (middle) and finally the linear combination (right).

For the reprojection step, the theoretical error is about 15%. This maximum will be reached at the border of the acquired images. After a closer look on the data (see Figure 9-left), this corresponds to pixels with low value in the acquired image, reducing the actual error. It can be seen on the projected images (see Figure 9-middle), where no noticeable difference is visible. For this light source, the acquisition system does not introduce a significant error.

For the linear combination step, we do not use an approximate dual representation, since the number of data is sufficiently low. We can notice in Figure 9-right that the data after the linear combination can be significantly different from the original one, as some large negative coefficients are introduced. Such approach guaranties a correct representation of the original radiance variation from the original light source, compared to traditional near-field photometry based on positive only data [Ash93, Ash95, RW97, JM00, SS96].

In order to show the accuracy, we compare the isolines of the projected pattern for both the real light source and the acquired one in Figure 10. The results are similar and more regular, due to the choice of the reconstruction basis. The approximations from the cylindrical case do not introduce an error that can be visually noticeable errors.

We also compute the projected pattern of the light at two different distances, as shown in Figure 11, in order to show that we manage to capture some near field effect. With only a goniometric diagram, the pattern would not change. Here, the pattern is changing with the distance.

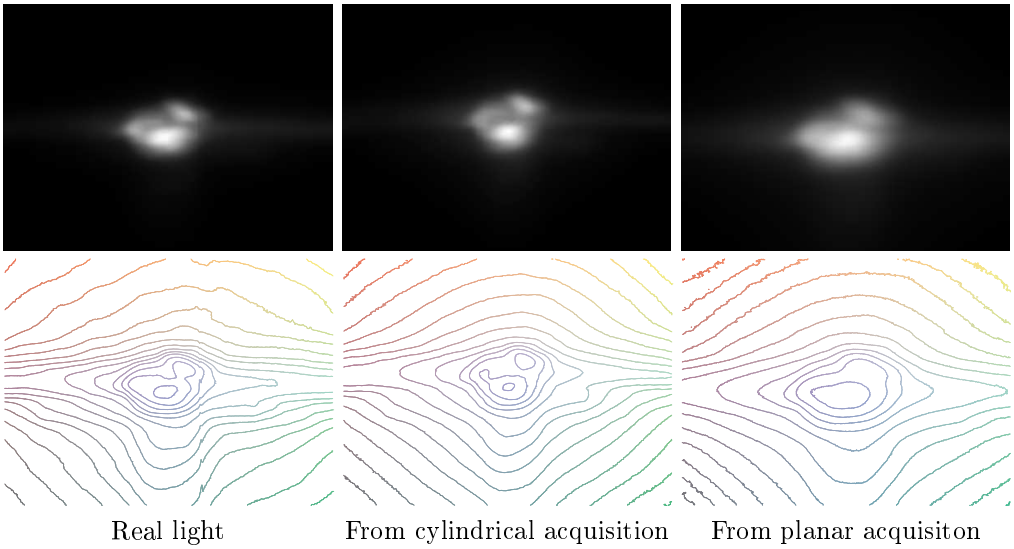

Figure 10: Comparison on the projected pattern of a car headlight (distance source-plane = 120 cm). A logarithmic scaled has been applied to the original intensities in order to create legible set of isolines. For each projected pattern, 15 isolines have been selected, in order to remove possible difference in maximum intensity between images, and focus only on the shape variation.

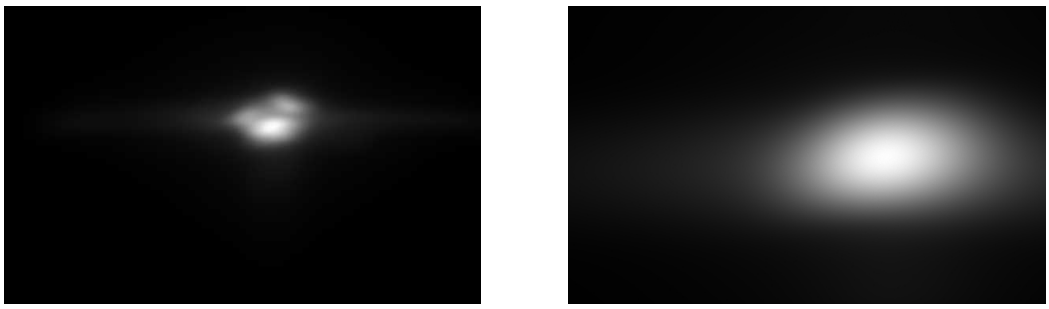

Figure 11: Projection on a wall parallel to the cylinder axis. The intensities have been scaled rescale to $[0, 1]$ in order to show the pattern variation with the distance (near-field effect). Left, distance source plane = 120 cm; right, distance source plane = 300 cm.

6.2 Planar Acquisition

In the planar acquisition, we test the acquisition with a smaller filter (2.73 mm). Note that with such a dimension, an error of alignment between two measures would have a larger

Figure 12: Global illumination solution

influence on the final results. Using a dual as a filter (and using one filter for its positive component and one for its negative one) is thus not be well suited for this configuration.

As the filter is smaller (i.e., we have a larger resolution), the number of measures has to be increased. The final data set is then an array of 23x15 (width x height) images, resulting in 1 GBytes of data. Such large data set would be very difficult to acquire without any automatic setups and without a single filter.

We do not use an approximation for the linear combination step, since it takes about 3.5 minutes to compute the linear combination on each resulting data (note that the computation was performed on an Intel Xeon 2.8GHz), and the full computation takes about 20 hours. By reducing the number of coefficients for the dual representation to 14, it would take only about 6.5 hours.

We can see that the projected pattern (see Figure 10) is also similar to the real light source, but more blurred. This leads to the following remark: for reaching the same quality in the near field representation, we need more measures at high resolution (i.e., with a smaller filter) for the planar case than for the cylindrical configuration, thanks to a more regular sampling in direction.

This data has also been used to compute a global illumination solution based on Photon Map algorithm[Jen01] - see Figure 12. For this simulation, the same light has been duplicated in order to create the two headlamps.

7 Conclusion

In this paper, we have presented a new acquisition system for complex light sources from the real world. This system is based on carefully designed optical filter. This filter allows performing an orthogonal projection of the light source in a selected basis.

The system has two components. The first step is the physical setup for the acquisition of optically filtered images, using the reconstruction basis function as a filter. In the second step, the data is processed on a computer to finalize the projection in the selected basis.

Two different setups have been experimented. In the first one, we use two planar supports for both the filters and the imaging device. The second one is based on a cylindrical support. This increases the regularity of the acquisition over one angular direction.

In order to bind the different errors (i.e., in the linear combination with an approximation of the dual basis function, in the cylindrical setup with the planar approximation of the filter and the measurement plane), we have presented a theoretical error study. This helps us in designing the final experimental setups.

In order to validate this approach, some results on the two setups have been presented. They consist in the acquisition of a car head-light. The results show that we manage to acquire both the near field and the far field of a light source, that the computation time of the linear combination is still reasonable, and that the resulting error of the planer approximation of the cylindrical setup is limited.

All these studies show that we can reach a good accuracy in light source acquisition using this simple optical filter design, and a high order basis.

7.1 Future Work

There are three main directions for future work. The first one consists in a closer look on the possible errors and a characterization of such acquisition device[RPN91]. Recall that the results presented here are very conservative bounds. With a closer analysis, we believe that the theoretical errors can be reduced.

The second direction is the extension of the cylindrical setup. This setup allows a better regularity of the acquisition in one angular dimension. It would be useful to not restrict this regularity to only one dimension. The best theoretical support for the acquisition would be two concentric spheres. Nevertheless, the design of a feasible setup for this configuration is more complex, and would require some careful approximations.

The third direction is to find a compact and memory-efficient representation. A compression scheme [AR97] for such light source models would make their usage more practical.

Acknowledgments

This work was funded by the PIMS (Pacific Institut for the Mathematical Sciences) Postdoctoral Fellowship program, and the INRIA (Institut National de Recherche en Informatique et en Automatique) associated laboratory program. The authors wish to thank David Roger, for his work on some aspects of the error study.

The authors can be contacted with the following emails: granier@labri.fr, goesele@mpi-sb.mpg.de, heidrich@cs.ubc.ca and hpseidel@mpi-sb.mpg.de.

Contents

References

[AR97] Ian Ashdown and Ron Rykowski. Making near-field photometry practical. In *1997 IESNA Conference Proceedings*, pages 368–389, Seattle, WA, August 1997. Illuminating Engineering Society of North America.

[Ash93] Ian Ashdown. Near-Field Photometry: A New Approach. *J. Illum. Eng. Soc.*, 22:163–180, Winter 1993.

[Ash95] Ian Ashdown. Near-Field Photometry: Measuring and Modeling Complex 3-D Light Sources. In *SIGGRAPH 95 Course Notes - Realistic Input for Realistic Images*, pages 1–15, Los Angeles, 1995. ACM Press.

[CCST00] Jin-Xiang Chai, Shing-Chow Chan, Heung-Yeung Shum, and Xin Tong. Plenoptic sampling. In *Proceedings of the 27th annual conference on Computer graphics and interactive techniques*, pages 307–318, New Orleans, 2000. ACM Press/Addison-Wesley Publishing Co.

[CJM02] William J. Cassarly, David R. Jenkins, and Holger Mönch. Accurate illumination system predictions using measured spatial luminance distributions. In C. Benjamin Wooley, editor, *Modeling and Characterization of Light Sources*, volume 4775, pages 78–85. SPIE, 2002.

[DM97] P. Debevec and J. Malik. Recovering High Dynamic Range Radiance Maps from Photographs. In *Computer Graphics Proceedings (SIGGRAPH 97)*, pages 369–378, Los Angeles, August 1997. ACM, ACM Press/Addison-Wesley Publishing Co.

[GGHS03] Michael Goesele, Xavier Granier, Wolfgang Heidrich, and Hans-Peter Seidel. Accurate light source acquisition and rendering. In *Proceedings of the SIGGRAPH 2003 annual conference*, San Antonio, July 2003. ACM Press.

[GGSC96] Steven J. Gortler, Radek Grzeszczuk, Richard Szelinski, and Michael F. Cohen. The Lumigraph. In *Computer Graphics Proceedings (SIGGRAPH 96)*, pages 43–54, New Orleans, August 1996. ACM Press/Addison-Wesley Publishing Co.

[Hal94] Michael W. Halle. Holographic stereograms as discrete imaging systems. In Stephen A. Benton, editor, *Practical Holography VIII*, volume 2176, pages 73–84. SPIE, February 1994.

[Jen01] Henrik Wann Jensen. *Realistic Image Synthesis Using Photon Mapping*. A. K. Peters, Natick, MA, 2001.

[JM00] David R. Jenkins and Holger Mönch. Source Imaging Goniometer Method of Light Source Characterization for Accurate Projection System Design. In *Proc. of SID (Society for Information Display) Conference*, pages 862–865, Long Beach, 2000.

[LaDP99] R. B. Lotto and S. M. Williams amd D. Purves. Mach bands as empirically derived associations. *Proc. Natl. Acad. Sci.*, 96(9):5245–5250, 1999.

[LH96] Marc Levoy and Pat Hanrahan. Light field rendering. In *Computer Graphics Proceedings (SIGGRAPH 96)*, pages 31–42, New Orleans, August 1996. ACM Press/Addison-Wesley Publishing Co.

[PLL+99] D. K. Pai, J. Lang, J. E. Lloyd, , and R. J. Woodham. ACME, A Telerobotic Active Measurement Facility. In *Proceedings of the Sixth International Symposium on Experimental Robotics*, Sydney, March 1999. Springer-Verlag.

[RBS99] M. A. Robertson, S. Borman, and R. L. Stevenson. Dynamic Range Improvement Through Multiple Exposures. In *Proc. of the Int. Conf. on Image Processing (ICIP'99)*, pages 159–163, Kobe, October 1999. IEEE.

[RPN91] Stephen E. Reichenbach, Stephen K. Park, and Ramkumar Narayanswamy. Characterizing digital image acquisition devices. *Optical Engineering*, 30(2):170–177, February 1991.

[RW97] Ronald F. Rykowski and C. Benjamin Wooley. Source Modeling for Illumination Design. In Robert E. Fischer, R. Barry Johnson, Richard C. Juergens, Warren J. Smith, and Paul R. Yoder Jr., editors, *Lens Design, Illumination, and Optomechanical Modeling*, volume 3130, pages 204–208. SPIE, 1997.

[SB90] S. Stannard and J. Brass. Application distance photometry. *J. Illum. Eng. Soc.*, 19:39–46, 1990.

[SS96] M. W. Siegel and R. D. Stock. A General Near-Zone Light Source Model and its Application to Computer Automated Reflector Design. *SPIE Optical Engineering*, 35(9):2661–2679, September 1996.

[VG84] C. P. Verbeck and D. P. Greenberg. A comprehensive light source description for computer graphics. *IEEE Computer Graphics & Applications*, 4(7):66–75, July 1984.

Unité de recherche INRIA Futurs
Parc Club Orsay Université - ZAC des Vignes
4, rue Jacques Monod - 91893 ORSAY Cedex (France)

Unité de recherche INRIA Lorraine : LORIA, Technopôle de Nancy-Brabois - Campus scientifique
615, rue du Jardin Botanique - BP 101 - 54602 Villers-lès-Nancy Cedex (France)
Unité de recherche INRIA Rennes : IRISA, Campus universitaire de Beaulieu - 35042 Rennes Cedex (France)
Unité de recherche INRIA Rhône-Alpes : 655, avenue de l'Europe - 38334 Montbonnot Saint-Ismier (France)
Unité de recherche INRIA Rocquencourt : Domaine de Voluceau - Rocquencourt - BP 105 - 78153 Le Chesnay Cedex (France)
Unité de recherche INRIA Sophia Antipolis : 2004, route des Lucioles - BP 93 - 06902 Sophia Antipolis Cedex (France)

Éditeur
INRIA - Domaine de Voluceau - Rocquencourt, BP 105 - 78153 Le Chesnay Cedex (France)
http://www.inria.fr
ISSN 0249-6399